

Neural Sensorless Control of Linear Induction Motors by a Full-Order Luenberger Observer Considering the End Effects

Angelo Accetta, *Member, IEEE*, Maurizio Cirrincione, *Senior Member, IEEE*, Marcello Pucci, *Senior Member, IEEE*, and Gianpaolo Vitale, *Senior Member, IEEE*

Abstract—This paper proposes a neural based full-order Luenberger adaptive speed observer for sensorless linear induction motor (LIM) drives, where the linear speed is estimated with the total least squares (TLS) EXIN neuron. A novel state space-vector representation of the LIM has been deduced, taking into consideration its dynamic end effects. The state equations of the LIM have been rearranged into a matrix form to be solved, in terms of the LIM linear speed, by any least squares technique. The TLS EXIN neuron has been used to compute online, in recursive form, the machine linear speed. A new gain matrix choice of the Luenberger observer, specifically taking into consideration the LIM dynamic end effects, has been proposed, overcoming the limits of the gain matrix choice based on the rotating-induction-machine model. The proposed TLS full-order Luenberger adaptive speed observer has been tested experimentally on an experimental rig. Results have been compared with those achievable with the TLS EXIN MRAS, the classic MRAS, and the sliding-mode MRAS observers.

Index Terms—Dynamic end effects, linear induction motor (LIM), Luenberger observer, neural networks (NNs), state model, total least squares (TLS).

NOMENCLATURE

$\mathbf{u}_s = u_{sD} + j u_{sQ}$	Inductor voltage space-vector in the inductor reference frame.
$\mathbf{i}_s = i_{sD} + j i_{sQ}$	Inductor current space-vector in the inductor reference frame.
$\mathbf{i}'_r = i_{rd} + j i_{rq}$	Induced part current space-vector in the inductor reference frame.

Manuscript received November 23, 2012; revised March 15, 2013 and July 30, 2013; accepted October 7, 2013. Date of publication November 4, 2013; date of current version May 15, 2014. Paper 2012-IDC-680.R2, presented at the 2012 IEEE Energy Conversion Congress and Exposition, Raleigh, NC, USA, September 15–20, and approved for publication in the IEEE TRANSACTIONS ON INDUSTRY APPLICATIONS by the Industrial Drives Committee of the IEEE Industry Applications Society. This work was supported by the following research projects: 1) RITmare, Ricerca Italiana per il mare (Italian Research for the sea) CUP: B91J11000740001; 2) TESEO, Tecnologie ad alta Efficienza per la Sostenibilit ergetica ed ambientale On-board (High efficiency technologies for on-board energy and environmental sustainability) CUP: B61C12000850005; 3) CNR per il Mezzogiorno (Advanced Technologies for Energy Efficiency and Sustainable Mobility) CUP: B51J10001290001.

A. Accetta, M. Pucci, and G. Vitale are with the Institute of Intelligent Systems for Automation (ISSIA-CNR), Palermo 90100, Italy (e-mail: angelo.accetta@ieee.org; marcello.pucci@ieee.org; gianpaolo.vitale@ieee.org).

M. Cirrincione is with the School of Engineering and Physics, University of the South Pacific at Suva, Fiji Islands (e-mail: cirrincione_m@usp.ac.fj).

Color versions of one or more of the figures in this paper are available online at <http://ieeexplore.ieee.org>.

Digital Object Identifier 10.1109/TIA.2013.2288429

$\psi_s = \psi_{sD} + j \psi_{sQ}$	Inductor flux space-vector in the inductor reference frame.
$\psi'_r = \psi_{rd} + j \psi_{rq}$	Induced part flux space-vector in the inductor reference frame.
L_S, L_R, L_M	Inductor, induced part, and three-phase magnetizing inductances.
$L_{\sigma s}, L_{\sigma r}$	Inductor and induced part leakage inductances.
R_s, R_r	Inductor and induced part resistances.
p	Number of pole pairs.
$\omega_r = (p\pi/\tau_p)v$	Equivalent angular speed of the induced part (in electrical angles per second).
ω_{mr}	Angular speed of the induced part flux (in electrical angles per second).
ρ_r	Angular position of the induced part flux.
v	Linear speed.
τ_m	Length of the inductor.
τ_p	Polar pitch.

I. INTRODUCTION

LINEAR induction motors (LIMs) have been attracting a lot of scientific interest for many years [1], [2]. The option that LIMs offer to develop a direct linear motion without the need of any gearbox for the motion transformation (from rotating to linear) has been the key issue for their study. The counterpart of this potential advantage is the increase of complexity of the machine model, which presents the so-called end effects and border effects. These effects, which are due to the absence of a cylindrical symmetry in the inductor structure with respect to the rotating machine, both in the longitudinal and in the transversal direction, are the cause of a limited capability of the LIM drive to achieve optimal performance. It calls for proper models that can suitably take into consideration these effects.

The speed control of the LIM, moreover, requires the adoption of a linear encoder, which is typically more expensive and less reliable than the corresponding counterpart in the rotating machine. As a matter of fact, in the LIM case, the cost of the encoder increases with the length of the induced part track, which could be very demanding in applications like railway traction systems and in general movement systems with long tracks where, typically, the linear encoder would also be exposed to potentially damaging environmental factors (sun, humidity, mechanical stress, etc.). Those considerations lead up to the need of adopting suitable sensorless techniques

[3], [4]. So far, very few applications of sensorless techniques for LIMs have been proposed in the literature, among which are those in [5] and [6], probably because of the increase of complexity of the speed observer, which should consider also the end effects of the machine. In particular, Huang *et al.* [5] propose a complex adaptive speed sensorless controller for the LIM, while Ryu *et al.* [6] propose a sensorless technique for LIMs based on the high frequency signal injection. In general, signal injection techniques are difficult to be applied to LIMs. From one side, the rotor slotting effect typically tracked in RIMs is absent in the induced part track (typical case of flat aluminum sheet secondary). From the other side, the saturation of the main flux is hard to be detected because of the big air-gap length making the LIM hardly saturable. Speed estimation is even worsened in this case by the high resistance of the induced part, resulting in very high percent slip speeds during LIM operation, and by the induced part time constant, which is variable with the position of the inductor because of the variable air gap. Cirrincione *et al.* [7] and Accetta *et al.* [8] propose a neural based MRAS observer, where the adaptive model is a linear neural network (NN) [total least squares (TLS) EXIN neuron], in numerical simulation and experimentally, respectively. This NN-based MRAS observer has been devised on the basis of a LIM dynamic model, including its dynamic end effects, resulting in better performance than the classic MRAS [9] and sliding mode (SM) MRAS observers [10] devised for rotating induction machines (RIMs), in terms of speed estimation accuracy.

This paper proposes a neural based full-order Luenberger adaptive speed observer, where the linear speed is estimated on the basis of the TLS EXIN neuron. A novel state space-vector representation of the LIM has been devised, considering its dynamic end effects; finally, the state equations of the LIM have been discretized and rearranged into a matrix form to be solved, in terms of the LIM linear speed, by any least squares (LS) technique. It has been then recognized that the speed computation corresponds more to an orthogonal regression problem, and for this reason, the TLS EXIN neuron has been employed to compute online and recursively the machine linear speed: indeed, it is the only NN able to solve online and in a recursive form the TLS problem [17]. A new choice of the gain matrix of the Luenberger observer, explicitly taking into consideration the LIM end effects, has been proposed, overcoming the limits of the choice of a gain matrix based on the RIM model. The proposed TLS full-order Luenberger adaptive speed observer has been assessed experimentally on a suitably developed test setup and compared with the TLS MRAS [8], the classic MRAS [9], and the SM-MRAS [10] observers. The proposed observer is the extension to the LIMs of the already proposed TLS full-order Luenberger speed observer, initially developed for RIMs [11]–[13]. It is noteworthy, however, that the method proposed here is not simply the straightforward application of a technique already developed for a RIM to a LIM: the whole state space-vector model, which is the core of the observer, has been analytically developed to consider also the dynamic end effects, making the observer suitable for LIM drives. As a consequence, the matrix equation suitable for the application of the TLS EXIN neuron has been properly rewritten. The observer has

been tested twice: with null gain matrix and with non-null gain matrix.

II. SPACE-VECTOR EQUIVALENT CIRCUIT OF THE LIM INCLUDING END EFFECTS

Unlike a RIM, in a single-sided LIM, the secondary (induced part) consists of a sheet of aluminum with a back core of iron. During the motion of the inductor, a continuous variation of the surface magnetically linked with the primary circuit occurs, since the inductor presents a limited length. This leads up to a variation of the induced currents in the sheet and the corresponding magnetic flux density in the air gap, close to the entrance (front of the motion) and exit (back of the motion) of the inductor. This flux in the entrance is different from the one in the exit. When the moving inductor comes across with a new part of aluminum sheet, new induced currents are generated starting from a null value. This generation is quite fast because of the absence of previously induced currents and tries to prevent the induced flux variation. The effect is a deep reduction of the resulting flux in the proximity of the entrance. At the same time, at the exit, the induced current opposes a sudden flux reduction from the inducer, creating an overall flux increase. In general, the higher the speed of the inductor, the higher the end effect phenomenon. This corresponds to the so-called “dynamic end effect” [1], and it has been taken into consideration in the literature by the “end effect factor Q ” [14], inversely proportional to the “goodness factor” defined in [1] as

$$Q = \frac{\tau_m R_r}{(L_m + L_{\sigma r})v}. \quad (1)$$

In general, the lower the value of Q , the higher the impact of the dynamic end effects.

From (1), it is apparent that Q decreases for an increase of the speed, an increase of the air-gap thickness (higher leakage inductance), or a decrease of the inductor length.

Correspondingly, the three-phase magnetizing inductance varies with Q in the following way:

$$\hat{L}_m = L_m (1 - f(Q)) \quad (2)$$

with

$$f(Q) = \frac{1 - e^{-Q}}{Q} \quad (3)$$

which states that the inductance value reduces with the increase of end effects (that is the inverse of Q).

A computation of the overall losses of the machine shows that an additional resistance appears in the transversal branch, taking into consideration the eddy current joule losses and accounting for the LIM braking force due to the dynamic end effects. This resistance is equal to

$$\hat{R}_r = R_r f(Q). \quad (4)$$

Correspondingly, the space-vector equivalent circuit of the LIM can be deduced (see Fig. 1). It can be observed that the main difference with the equivalent circuit of the RIM is in the magnetizing inductance and in the eddy current resistance, both present in the transversal branch.

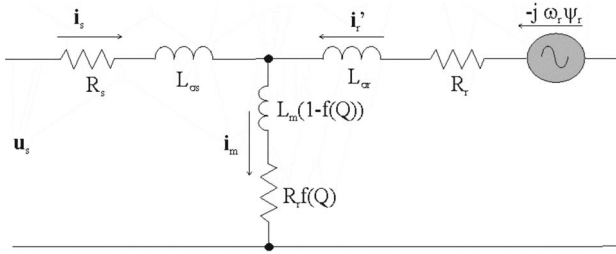


Fig. 1. Space-vector equivalent circuit of the LIM in the inductor reference frame.

III. TLS-BASED FULL-ORDER SPEED OBSERVER INCLUDING END EFFECTS

A. Space-Vector State Equations of the LIM

Starting from the space-vector equivalent circuit in the inductor reference frame in Fig. 1, after applying the Kirchhoff law, the following set of space-vector equations of the LIM can be written in the inductor reference frame:

$$\begin{cases} \mathbf{u}_s = R_s \mathbf{i}_s + R_r f(Q) [\mathbf{i}_s + \mathbf{i}'_r] + \frac{d\psi_s}{dt} & (5a) \\ \mathbf{0} = R_r \mathbf{i}'_r + R_r f(Q) [\mathbf{i}_s + \mathbf{i}'_r] + \frac{d\psi'_r}{dt} - j\omega_r \psi'_r & (5b) \end{cases}$$

with

$$\begin{cases} \psi_s = [L_{\sigma s} + L_m(1 - f(Q))] \mathbf{i}_s + L_m(1 - f(Q)) \mathbf{i}'_r & (6a) \\ \psi'_r = L_m(1 - f(Q)) \mathbf{i}_s + [L_{\sigma r} + L_m(1 - f(Q))] \mathbf{i}'_r & (6b) \end{cases}$$

where \mathbf{u}_s , \mathbf{i}_s , \mathbf{i}'_r , ψ_s , and ψ'_r are respectively the inductor voltage and current, the induced part current, and the inductor and induced part flux linkage space-vectors written in the inductor reference frame, R_s and R_r are the inductor and induced part phase resistances, $L_{\sigma s}$ and $L_{\sigma r}$ are the inductor and induced part leakage inductances, ω_r is the electrical rotating speed of the inductor, Q is the previously defined end effect factor, and j is the imaginary unit. Equations (5a) and (5b) are respectively the inductor and induced part voltage equations, while (6a) and (6b) are respectively the inductor and induced part flux equations. Writing (6b) as a function of \mathbf{i}'_r and substituting it in (5a), the space-vector equations of the voltage model of the LIM can be deduced

$$\begin{aligned} \frac{d\psi'_r}{dt} &= \frac{L_{\sigma r} + L_m(1 - f(Q))}{L_m(1 - f(Q))} \\ &\times \left\{ \mathbf{u}_s - \left[R_s + R_r f(Q) - \frac{R_r f(Q) L_m(1 - f(Q))}{L_{\sigma r} + L_m(1 - f(Q))} \right] \mathbf{i}_s \right. \\ &\quad - \hat{\sigma} [L_{\sigma s} + L_m(1 - f(Q))] \frac{d\mathbf{i}_s}{dt} \\ &\quad \left. - \frac{R_r f(Q)}{L_{\sigma r} + L_m(1 - f(Q))} \psi'_r \right\} \end{aligned} \quad (7)$$

where $\hat{\sigma}$ has been previously defined as

$$\hat{\sigma} = 1 - \frac{L_m^2(1 - f(Q))^2}{[L_{\sigma r} + L_m(1 - f(Q))][L_{\sigma s} + L_m(1 - f(Q))]}.$$

$\hat{\sigma}$ is an equivalent global leakage factor, taking into consideration the end effects of the LIM.

Equation (7) has been deduced under the simplifying assumption that the rate of change of the linear speed is limited, i.e., $dv/dt \cong 0$; otherwise, some additive terms depending on the linear acceleration of the motor would appear. This implies that the mechanical acceleration of the motor is not considered only limited to the fast parameter variation. It is considered therefore the variation of the parameters with the LIM speed while the effect of the acceleration on the parameters is neglected. This simplifying assumption is reasonable since the mechanical time constant is much bigger than the electric one. This is particularly true for LIMs where the inductance terms are all very small because of the big air gap and the resistances are big, particularly that of the induced part track (limited thickness of the track).

Writing (6b) as a function of \mathbf{i}'_r and substituting it in (5b), the space-vector equations of the current model can be deduced

$$\begin{aligned} \frac{d\psi'_r}{dt} &= R_r \left(\frac{L_m(1 - f(Q))(1 + f(Q))}{L_{\sigma r} + L_m(1 - f(Q))} - f(Q) \right) \mathbf{i}_s \\ &\quad + \left(j \frac{p\pi}{\tau_p} v - \frac{R_r(1 + f(Q))}{L_{\sigma r} + L_m(1 - f(Q))} \right) \psi'_r \end{aligned} \quad (8)$$

where τ_p is the polar step of the inductor and p is the number of pole pairs. Even in this case, (8) has been deduced under the simplifying assumption that the rate of change of the linear speed is limited, i.e., $dv/dt \cong 0$.

From (8), an equivalent induced part time constant of the machine taking into consideration the end effects, depending on the linear machine speed itself, can be defined as

$$\hat{T}_r = \frac{L_{\sigma r} + L_m(1 - f(Q))}{R_r(1 + f(Q))}. \quad (9)$$

To obtain the full-order Luenberger observer, a state space-vector representation should be deduced. From this standpoint, (5) and (6) have been properly manipulated so as to obtain the state representation of the LIM including the end effects.

For the sake of simplicity, the following modified electrical parameters of the LIM (variable with the machine speed) are defined:

$$\hat{L}_s = L_{\sigma s} + L_m(1 - f(Q)) \quad (10a)$$

$$\hat{L}_r = L_{\sigma r} + L_m(1 - f(Q)) \quad (10b)$$

permitting the state model to be rewritten in a more compact form. These parameters can be considered as the generalized version of the machine parameters and clearly have a physical meaning. To deduce the state representation of the space-vector model of the LIM taking into consideration the end effects, the first space-vector equation to be considered is the voltage model represented in (7), which must be rewritten as a function of $d\mathbf{i}_s/dt$, after substituting the expression of $d\psi'_r/dt$ taken from the current model of (8). The second space-vector equation is given directly by the current model, given by (8). As a

result, the following set of two space-vector equations can be obtained:

$$\frac{d\mathbf{i}_s}{dt} = \frac{1}{\hat{\sigma}\hat{L}_s} \left\{ \mathbf{u}_s - \left[R_s + \hat{R}_r \left(1 - \frac{\hat{L}_m}{\hat{L}_r} \right) + \frac{\hat{L}_m}{\hat{L}_r} \left(\frac{\hat{L}_m}{\hat{T}_r} - \hat{R}_r \right) \right] \mathbf{i}_s + \frac{\hat{L}_m}{\hat{L}_r} \left[j \frac{p\pi}{\tau_p} v - \frac{1}{\hat{T}_r} - \frac{\hat{R}_r}{\hat{L}_m} \right] \boldsymbol{\psi}'_r \right\} \quad (11)$$

$$\frac{d\boldsymbol{\psi}'_r}{dt} = \left[\frac{\hat{L}_m}{\hat{T}_r} - \hat{R}_r \right] \mathbf{i}_s + \left[j \frac{p\pi}{\tau_p} v - \frac{1}{\hat{T}_r} \right] \boldsymbol{\psi}'_r \quad (12)$$

which can also be written as

$$\frac{d}{dt} \begin{bmatrix} \mathbf{i}_s \\ \boldsymbol{\psi}'_r \end{bmatrix} = \begin{bmatrix} \mathbf{A}_{11} & \mathbf{A}_{12} \\ \mathbf{A}_{21} & \mathbf{A}_{22} \end{bmatrix} \begin{bmatrix} \mathbf{i}_s \\ \boldsymbol{\psi}'_r \end{bmatrix} + \begin{bmatrix} \mathbf{B}_1 \\ \mathbf{0} \end{bmatrix} \mathbf{u}_s = \mathbf{A}\mathbf{x} + \mathbf{B}\mathbf{u}_s \quad (13a)$$

$$\mathbf{i}_s = \mathbf{C}\mathbf{x} \quad (13b)$$

where $\mathbf{C} = [\mathbf{I} \ \mathbf{0}]$, $\mathbf{I} = \begin{bmatrix} 1 & 0 \\ 0 & 1 \end{bmatrix}$, $\mathbf{J} = \begin{bmatrix} 0 & -1 \\ 1 & 0 \end{bmatrix}$, and

$$\begin{aligned} \mathbf{A}_{11} &= a_{11}\mathbf{I} \\ &= -\frac{1}{\hat{\sigma}\hat{L}_s} \left[R_s + \hat{R}_r \left(1 - \frac{\hat{L}_m}{\hat{L}_r} \right) + \frac{\hat{L}_m}{\hat{L}_r} \left(\frac{\hat{L}_m}{\hat{T}_r} - \hat{R}_r \right) \right] \mathbf{I} \end{aligned} \quad (14a)$$

$$\begin{aligned} \mathbf{A}_{12} &= \hat{a}_{12} \left[\left(\frac{1}{\hat{T}_r} + \frac{\hat{R}_r}{\hat{L}_m} \right) \mathbf{I} - \frac{p\pi}{\tau_p} v \mathbf{J} \right] \\ &= \frac{\hat{L}_m}{\hat{\sigma}\hat{L}_s\hat{L}_r} \left[\left(\frac{1}{\hat{T}_r} + \frac{\hat{R}_r}{\hat{L}_m} \right) \mathbf{I} - \frac{p\pi}{\tau_p} v \mathbf{J} \right] \end{aligned} \quad (14b)$$

$$\mathbf{A}_{21} = \hat{a}_{21}\mathbf{I} = \left(\frac{\hat{L}_m}{\hat{T}_r} - \hat{R}_r \right) \mathbf{I} \quad (14c)$$

$$\mathbf{A}_{22} = \hat{a}_{22} \left[\frac{1}{\hat{T}_r} \mathbf{I} - \frac{p\pi}{\tau_p} v \mathbf{J} \right] = -1 \left[\frac{1}{\hat{T}_r} \mathbf{I} - \frac{p\pi}{\tau_p} v \mathbf{J} \right] \quad (14d)$$

$$\mathbf{B}_1 = \hat{b}_1\mathbf{I} = \frac{1}{\hat{\sigma}\hat{L}_s} \mathbf{I} \quad (14e)$$

It can easily be observed that, if the end effects were neglected ($f(Q) = 0$), the coefficients of the LIM state space-vector equation would coincide with those of the classic RIM [11]–[13], [15].

B. Full-Order Luenberger Observer

The full-order Luenberger observer is a deterministic state observer estimating the inductor current and the induced part flux linkages. It is described by the following equations:

$$\frac{d\hat{\mathbf{x}}}{dt} = \hat{\mathbf{A}}\hat{\mathbf{x}} + \mathbf{B}\mathbf{u}_s + \mathbf{G}(\hat{\mathbf{i}}_s - \mathbf{i}_s) \quad (15)$$

where $\hat{\mathbf{x}}$ means the estimated values (not to be confused with the speed varying parameters as explained above) and \mathbf{G} is the observer gain matrix which must be designed so that the observer is stable. The matrix \mathbf{G} acts on the inductor current estimation error since the inductor current is only a portion of the state vector that is a measurable quantity. For the choice of the gain matrix, two solutions have been explored. Initially, for the sake of simplicity, $\mathbf{G} = \mathbf{0}$ has been set. In this case, the dynamics of the observer coincides with that of the machine, and no feedback action exists. Afterward, the gain matrix has been chosen following the criterion in [15], whereby the poles of the observer are proportional to the machine poles. It should be remarked that the observer gain matrix expression in [15] has been developed for the RIM. Here, under the same criterion, a new gain matrix expression has been found which takes into consideration the LIM dynamic end effects.

If λ is the proportionality factor ($\lambda \geq 1$) between the observer and the machine poles, the following terms of the gain matrix \mathbf{G} can be found:

$$\mathbf{G} = \begin{bmatrix} \hat{g}_1 & -\hat{g}_2 \\ \hat{g}_2 & \hat{g}_1 \\ \hat{g}_3 & -\hat{g}_4 \\ \hat{g}_4 & \hat{g}_3 \end{bmatrix} \quad (16)$$

where (17), shown at the bottom of the page, is obtained with

$$\hat{c} = -\frac{\hat{\sigma}\hat{L}_s\hat{L}_r}{\hat{L}_m} \quad (18)$$

$$\hat{d} = \frac{\beta}{\Re(\hat{a}_{12})^2 + \Im(\hat{a}_{12})^2} \quad (19)$$

with $\beta = \hat{R}_r/\hat{L}_m$.

It should be remarked that (17), even if developed under the same observer pole location as in [15], is quite different from [15, (10)–(13)] because of the presence of some additive terms which are multiplied for \hat{d} . Since \hat{d} is proportional to \hat{R}_r , which is an additive term not present in the RIM equivalent electrical circuit but is linked to the LIM dynamic end effects (null for zero machine speed), by setting $\hat{d} = 0$, the

$$\begin{cases} \hat{g}_1 = (\lambda - 1) [\Re(\hat{a}_{11}) + \Re(\hat{a}_{22})] \\ \hat{g}_2 = (\lambda - 1) \Im(\hat{a}_{22}) \\ \hat{g}_3 = (\lambda - 1) \left\{ \hat{c} [\Re(\hat{a}_{11}) + \Re(\hat{a}_{22})] + \hat{d} [\Re(\hat{a}_{12}) (\Re(\hat{a}_{11}) + \Re(\hat{a}_{22})) + \Im(\hat{a}_{22}) \Im(\hat{a}_{12})] \right\} \\ \quad - (\lambda^2 - 1) \left\{ [\hat{c} \Re(\hat{a}_{11}) - \Re(\hat{a}_{21})] + \hat{d} \Re(\hat{a}_{11}) \Re(\hat{a}_{12}) \right\} \\ \hat{g}_4 = (\lambda - 1) \left\{ \hat{c} \Im(\hat{a}_{22}) - \hat{d} [\Im(\hat{a}_{12}) (\Re(\hat{a}_{11}) + \Re(\hat{a}_{22})) - \Im(\hat{a}_{22}) \Re(\hat{a}_{12})] \right\} - (\lambda^2 - 1) \left\{ \hat{d} \Re(\hat{a}_{11}) \Im(\hat{a}_{12}) \right\} \end{cases} \quad (17)$$

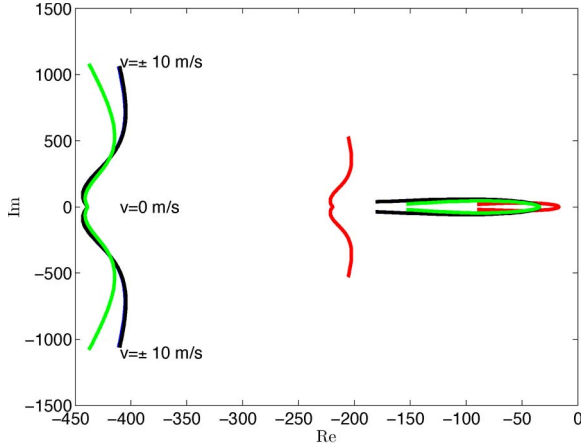


Fig. 2. (Red) LIM machine poles, (blue) observer ideal LIM poles, (black) observer actual LIM poles, and observer actual RIM poles, with $\lambda = 2$.

corresponding RIM gain matrix described by [15, (10)–(13)] is obtained.

It should, in any case, be borne in mind that the all \hat{a}_{ij} terms in (17) are those of the LIM model, depending on the LIM speed and thus taking into consideration the dynamic end effects.

Fig. 2 shows the variation with the LIM speed, in a speed range from -10 m/s to 10 m/s (LIM rated speed equal to 6.8 m/s), of the following variables:

- 1) LIM poles (red), corresponding to the eigenvalues of the \mathbf{A} matrix in (14);
- 2) ideal observer poles obtained under the assumption of perfect proportionality with the LIM poles (blue), with $\lambda = 2$;
- 3) actual observer poles obtained with the gain matrix choice taking into consideration the LIM dynamic end effects (black), with $\lambda = 2$;
- 4) actual observer poles obtained with the classic gain matrix choice developed for the RIM, not taking into consideration the LIM dynamic end effects (black), with $\lambda = 2$.

It should be noted that the proposed gain matrix choice in (17) considering the LIM end effects permits the actual observer poles (black) to perfectly match the ideal ones (blue). On the contrary, the adoption in the LIM case of the classic gain matrix choice developed for the RIM (black) leads to a deformation of the observer poles with respect to the ideal ones. In practice, the adoption of the gain matrix developed for RIMs corresponds to considering the observer to be more overdamped than in the case in which the gain matrix choice is made considering the end effects. It should be finally noted

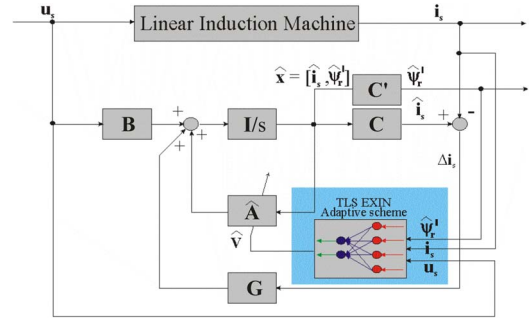


Fig. 3. Block diagram of the TLS full-order Luenberger observer.

that, in the LIM under test, differently from the classic rotating machine case, the poles related to the inductor current lie more on the right than those related to the induced part flux linkage (they are slower). This is caused by the very low value of the induced part inductance and the high value of its resistance. In particular, the inductor current dynamics is only slightly modified by this gain matrix selection, unlike the ideal case.

C. TLS Speed Adaptation Law

The TLS speed adaptation law derives from a modification of (13), in the sense that it exploits the two first scalar equations to estimate the rotor speed, after transforming them into discrete form for digital implementation [11]–[13]. Moving from the continuous domain to the discrete one and approximating the continuous derivative with the discrete filter $((1 - z^{-1})/(T_s z^{-1}))$, where T_s is the sampling time of the control systems, the matrix equation (20), shown at the bottom of the page, can be deduced.

More details on the derivation of (20) are provided in Appendix.

Equation (19) is a classical matrix equation of the type $\mathbf{Ax} \approx \mathbf{b}$, where \mathbf{A} is called “data matrix,” \mathbf{b} is called “observation vector,” and \mathbf{x} is the unknown vector, equal to the estimated linear speed \hat{v} .

LS techniques can be adopted for the online training of the corresponding linear NN (ADALINE) and for solving in a recursive form this equation [17]. Among the different types of LS techniques (OLS = Ordinary Least Squares, TLS = Total Least Squares, and DLS = Data Least Squares), TLS reveals intrinsically the best to solve the problem of speed estimation. As a matter of fact, the data matrix \mathbf{A} is composed of the D-Q axis components of the estimated induced part flux linkage, which is affected by errors resulting from an imperfect tuning of the observer (parameter uncertainty) and noise from

$$\begin{aligned} & \begin{bmatrix} \hat{a}_{12} T_s \frac{p\pi}{\tau_p} \hat{\psi}_{rq}(k-1) \\ -\hat{a}_{12} T_s \frac{p\pi}{\tau_p} \hat{\psi}_{rd}(k-1) \end{bmatrix} \hat{v}(k-1) \\ & = \begin{bmatrix} i_{sD}(k) - i_{sD}(k-1) - \hat{a}_{11} T_s i_{sD}(k-1) - \hat{a}_{12} \left(\frac{1}{T_r} + \frac{\hat{R}_r}{\hat{L}_m} \right) T_s \hat{\psi}_{rd}(k-1) - \hat{b}_1 T_s \hat{u}_{sD}(k-1) \\ i_{sQ}(k) - i_{sQ}(k-1) - \hat{a}_{11} T_s i_{sQ}(k-1) - \hat{a}_{12} \left(\frac{1}{T_r} + \frac{\hat{R}_r}{\hat{L}_m} \right) T_s \hat{\psi}_{rq}(k-1) - \hat{b}_1 T_s \hat{u}_{sQ}(k-1) \end{bmatrix} \end{aligned} \quad (20)$$



Fig. 5. Photograph of the experimental test setup.

TABLE I
PARAMETERS OF THE LIM

Rated power P_{rated} [W]	424.7
Rated voltage U_{rated} [V]	380
Rated frequency f_{rated} [Hz]	60
Pole-pairs	3
Inductor resistance R_s [Ω]	11
Inductor inductance L_s [mH]	637.6
Induced part resistance R_r [Ω]	32.57
Induced part inductance L_r [mH]	757.8
3-phase magnetizing inductance L_m [mH]	517.5
Rated thrust F_n [N]	200
Rated speed [m/s]	6.85
Mass [kg]	20

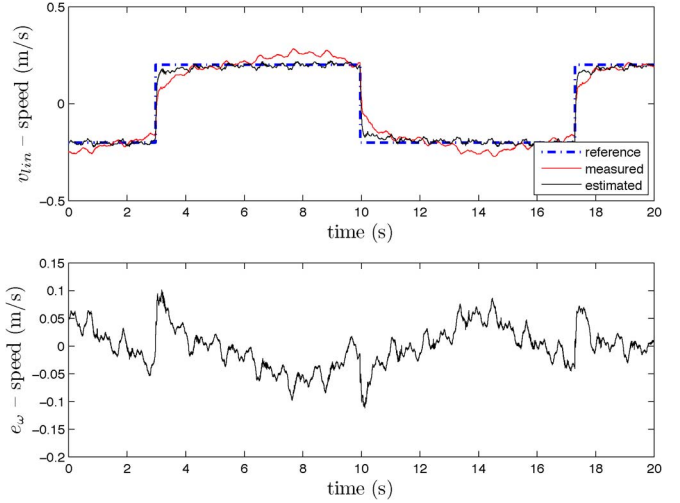
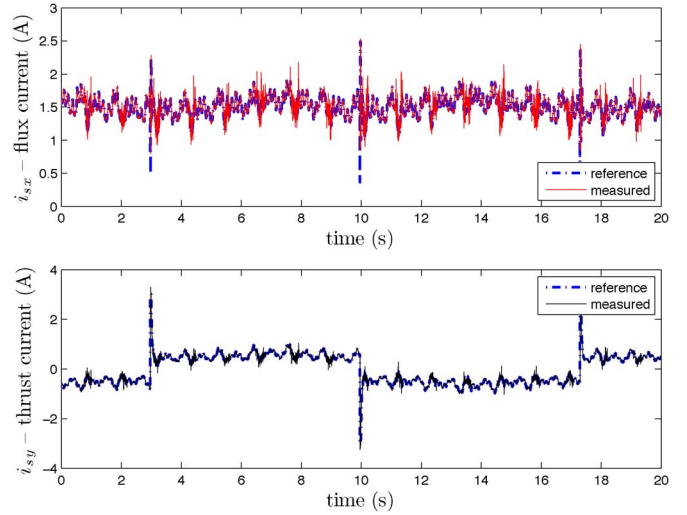
the LIM drive has been operated with the estimated speed fed back to the speed control loop, while the measured speed has been used only for comparison.

A. Null Gain Matrix

All the results provided in this section refer to the case of the null gain matrix. The first test corresponds to a set of speed reversals at very low speed, from 0.2 to -0.2 m/s (the rated linear speed of the LIM is 6.85 m/s), corresponding to almost 3% of the rated speed. The frequency of the square speed reference is determined by the length of the track: Whenever the inductor reaches the end of the track, the sign of the speed reference is changed.

Fig. 6 shows the reference, the estimated, and the measured speed as well as the speed estimation error during this test. The estimated speed properly tracks its reference and the measured one, with a transient estimation error (peak error almost equal to 0.1 m/s) depending on the inductor position on the track.

With this specific regard, it should be noted that, differently from the RIM where the air gap can be considered almost uniform or very slightly variable because of the construction tolerances, in the LIM case, the air-gap length presents significant variations along its path, which imply modifications of the magnetizing inductance with the inductor position causing a different accuracy of the speed estimation along the track, even at steady-state speed. In addition, not only the speed reference is very low, but also, the LIM drive is actually loaded (almost 30% of the rated load with a very high slip because of the high

Fig. 6. Reference, estimated, and measured linear speeds during the $0.2 \rightarrow -0.2$ step with the null gain matrix (experiment).Fig. 7. i_{sx} , i_{sy} reference and measured current components during the $0.2 \rightarrow -0.2$ step with the null gain matrix (experiment).

value of the induced part resistance), just because of the friction force of the system due to the inductor wheels rotating on the lateral tracks shown in Fig. 5.

Fig. 7 shows the corresponding i_{sx} , i_{sy} current components. They highlight a proper field orientation, with i_{sx} correctly controlled to a constant value and i_{sy} suddenly varying at each speed reversal and controlled to a constant non-null value at steady-state speed (due to the load).

Figs. 8 and 9 show respectively the time variation of the modified electrical parameters (\hat{R}_r , \hat{L}_m , \hat{T}_r) of the LIM and its state model parameters (\hat{a}_{11} , \hat{a}_{12} , \hat{a}_{21} , \hat{a}_{22} , \hat{b}_1). The modified electrical parameters of the LIM vary with the speed, as expected, according to (2), (4), and (10), maintaining a constant value during steady-state speed while varying during each transient speed. The dynamics of both the electrical and the state parameter variations coincides with that of the mechanical speed of the LIM [see (2), (4), and (9)], and in this case, more precisely with that of the estimated speed, which is very close but not exactly equal to that of the real LIM.

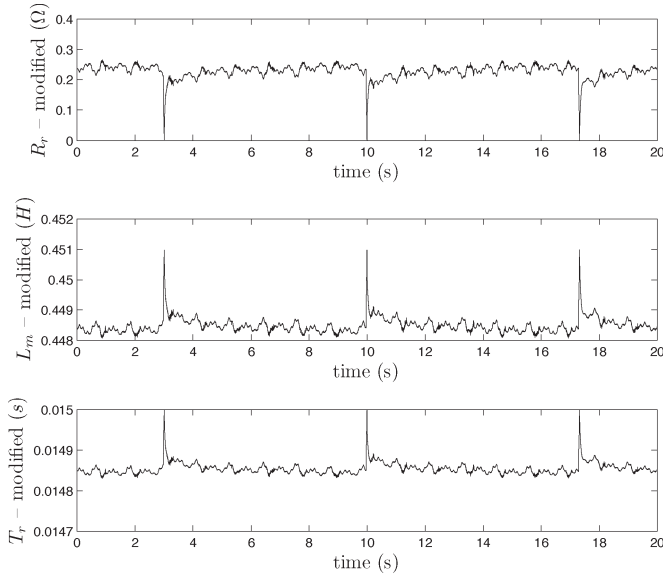


Fig. 8. Modified electrical parameters during the 0.2 → -0.2 step with the null gain matrix (experiment).

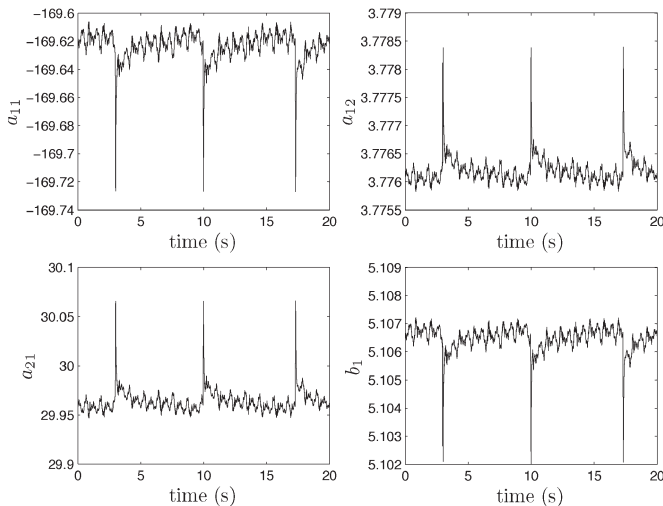


Fig. 9. Modified state model parameters during the 0.2 → -0.2 step with the null gain matrix (experiment).

As expected, \hat{R}_r increases with the speed, while \hat{L}_m and \hat{T}_r reduce with it. Similar considerations are valid for the state model parameters, which vary with the speed of the LIM in accordance with (14). As expected, \hat{a}_{11} and \hat{b}_1 increase with the speed, while \hat{a}_{12} and \hat{a}_{21} decrease with it. It should be noted that the variations of both the electrical and state parameters with speed are limited. It is due to the limited variation of the speed during the test and to the limited presence of the dynamic end effects in the LIM under test (not high value of Q).

Afterward, a start-up plus speed reversal and a speed reversal plus stopping test have been performed. The start-up test consists of the following speed step references: 0 → -0.6 → 0.6 m/s. On the other hand, the braking one consists of the following speed step reference: -0.6 → 0.6 → 0 m/s. Both tests are particularly challenging since they imply a speed reversal at medium speed, a speed transient from/to zero speed, and a long period in which the drive is driven at zero speed with

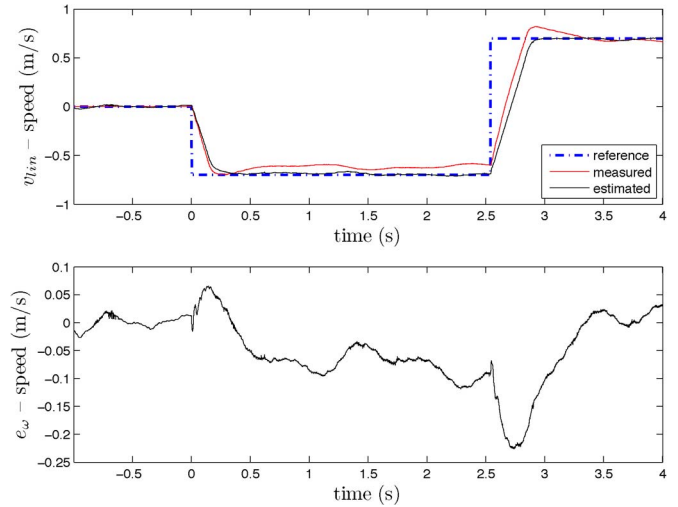


Fig. 10. Reference, estimated, and measured linear speeds during the start-up test with the null gain matrix (experiment).

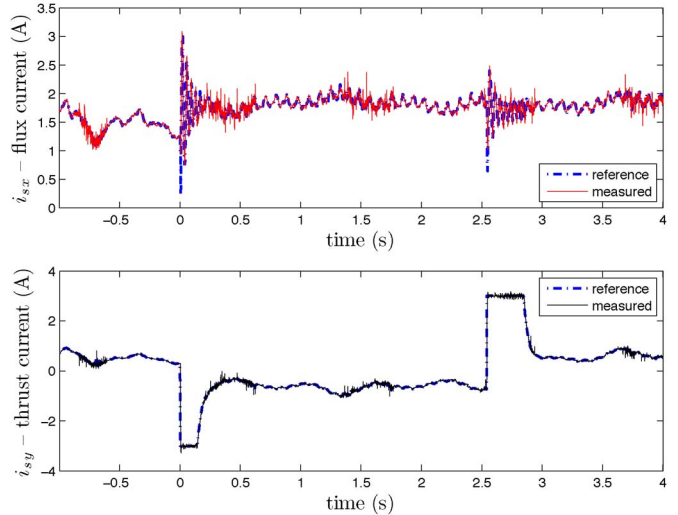


Fig. 11. i_{sx} , i_{sy} reference and measured current components during the start-up test with the null gain matrix (experiment).

the LIM fully magnetized. Fig. 10 (13) shows the reference, the estimated, and the measured speed as well as the speed estimation error during the start-up (braking) test, respectively. Fig. 11 (14) shows the corresponding waveforms of the reference and measured i_{sx} , i_{sy} current components. Fig. 12 (15) shows the corresponding waveforms of the measured and estimated i_{sD} , i_{sQ} current components.

Figs. 10–15 show the capability of the TLS full-order Luenberger observer to properly track these speed references with a good accuracy even in transient, being able to work at zero speed with the machine fully magnetized. Figs. 12 and 15 show that the estimated current components track the measured ones, even if with an estimation error due to the imperfect tuning of the observer and the null gain matrix choice. The accuracy in the inductor current estimation is significantly improved if a non-null gain matrix is adopted, as shown in the following. Finally, a significant ripple appears on the i_{sx} current component (see Fig. 14), particularly in the entire time interval when the speed reference is null. During this working condition (zero

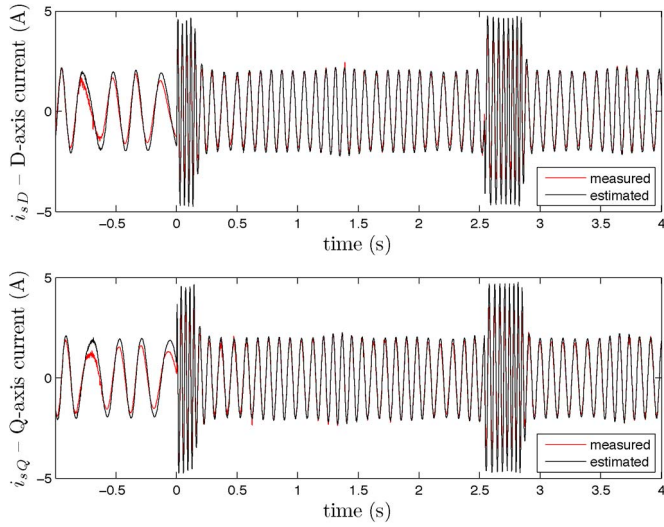


Fig. 12. i_{sD} , i_{sQ} estimated and measured current components during the start-up test with the null gain matrix (experiment).

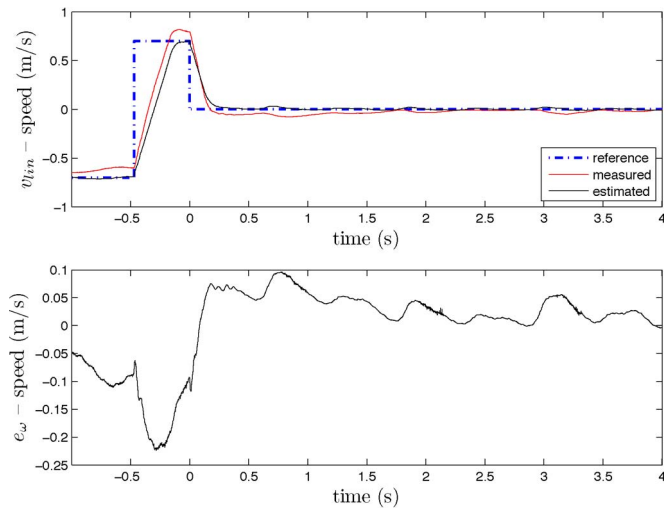


Fig. 13. Reference, estimated, and measured linear speeds during the stopping test with the null gain matrix (experiment).

speed at no load), the LIM speed is theoretically unobservable. The TLS EXIN neuron is able to estimate the speed and to make the LIM drive work at zero speed since it exploits the dynamic equations of the LIM. Whenever the speed becomes slightly different from zero, the TLS EXIN neuron is able estimate it, and the control system can make a correction action to force the LIM to work at zero speed. It means that, around zero speed, the estimated speed presents more ripple and, consequently, the state observer behavior is more critical. Even the estimation of the induced part flux angle suffers from this condition with consequent worsening of the field orientation condition, which accounts for the ripple on the i_{sx} current component.

B. Non-Null Gain Matrix

All the results provided in this section refer to the case of the gain matrix choice described in Section III-B. As a consequence of the adoption of a non-null gain matrix, the accuracy of the state variables and speed estimation improves,

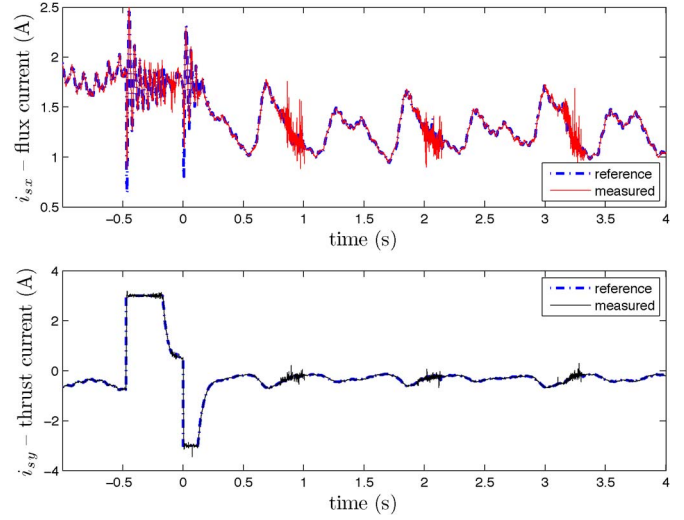


Fig. 14. i_{sx} , i_{sy} reference and measured current components during the stopping test with the null gain matrix (experiment).

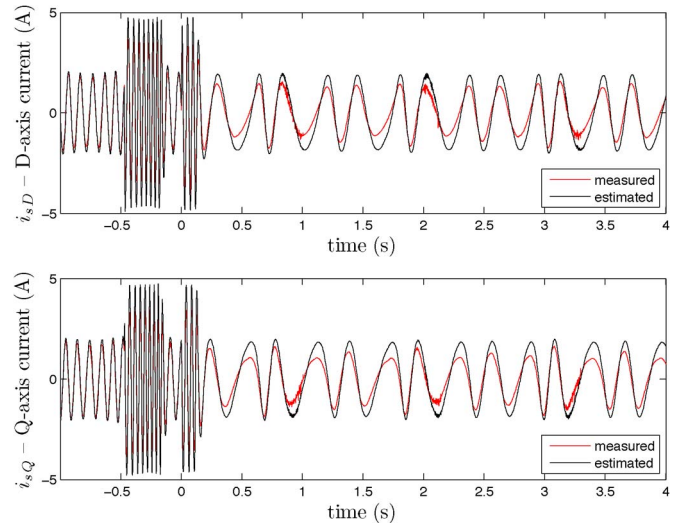


Fig. 15. i_{sD} , i_{sQ} estimated and measured current components during the stopping test with the null gain matrix (experiment).

and consequently, the minimum working speed becomes lower: 0.1 m/s against 0.2 m/s, corresponding to almost 1.4% of the rated speed, as demonstrated in the following. Fig. 16 shows the reference, estimated, and measured speeds during the 0.1-m/s square speed reference waveform. The estimated speed properly tracks its reference and the measured one, even if with a transient estimation error (peak error almost equal to 0.05 m/s) depending on the inductor position on the track (see aforementioned comment). Fig. 17 shows the corresponding i_{sx} , i_{sy} current components that highlight a proper field orientation, with i_{sx} correctly controlled to a constant value and i_{sy} suddenly varying at each speed reversal and controlled to a constant non-null value at steady-state speed (due to the load). These curves present slight oscillations tracking the oscillation of the estimated speed, as expected due to the very low speed sensorless operation. Fig. 18 shows the corresponding waveforms of the i_{sD} , i_{sQ} estimated and measured current components. It clearly highlights that the adoption of a non-null gain matrix permits a more accurate estimation of the

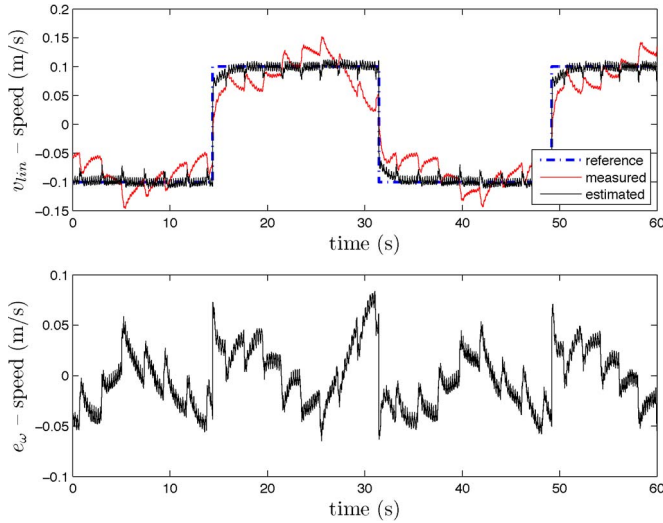


Fig. 16. Reference, estimated, and measured linear speeds during the 0.1 \rightarrow -0.1 step with the non-null gain matrix (experiment).

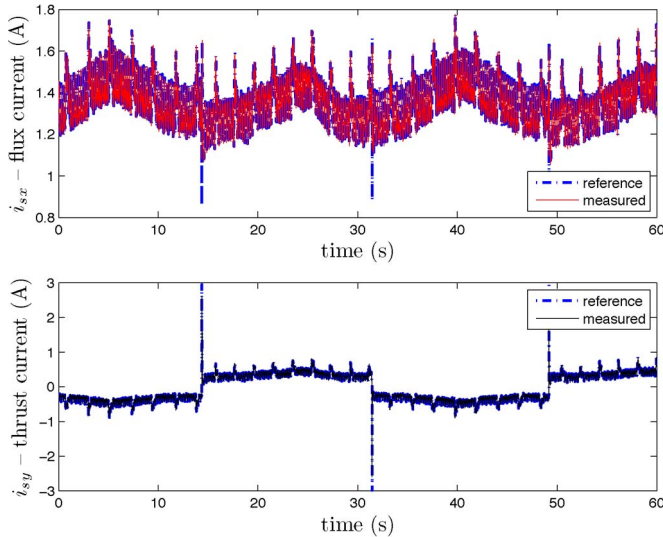


Fig. 17. i_{sx} , i_{sy} reference and measured current components during the 0.1 \rightarrow -0.1 step with the non-null gain matrix (experiment).

inductor currents, as expected. Finally, a speed reference composed of the following subsequent steps at very low speed has been given to the drive: $-0.1 \rightarrow 0.1 \rightarrow 0.2 \rightarrow -0.2 \rightarrow 0.2 \rightarrow 0.3 \rightarrow -0.3 \rightarrow -0.3 \rightarrow -0.3$ m/s. Fig. 19 shows the speed waveforms, Fig. 20 shows the i_{sx} , i_{sy} current components, Fig. 21 shows the i_{sD} , i_{sQ} estimated and measured current components, Fig. 22 shows the modified electrical parameters, and finally, Fig. 23 shows the modified state parameters during this test. These figures show a good tracking capability of the estimated speed that follows its reference and the measured speed during steps of different amplitude and sign. Each of the zero crossings of the speed is performed quite quickly, even if all transients are performed at very low speed. Correspondingly, the i_{sx} is maintained constant corresponding to the magnetization level of the machine, and i_{sy} tracks the variations of the speed reference. The higher the speed reference, the higher the i_{sy} since the friction load torque increases (with nonlinear law) with the working speed. The modified electrical and state

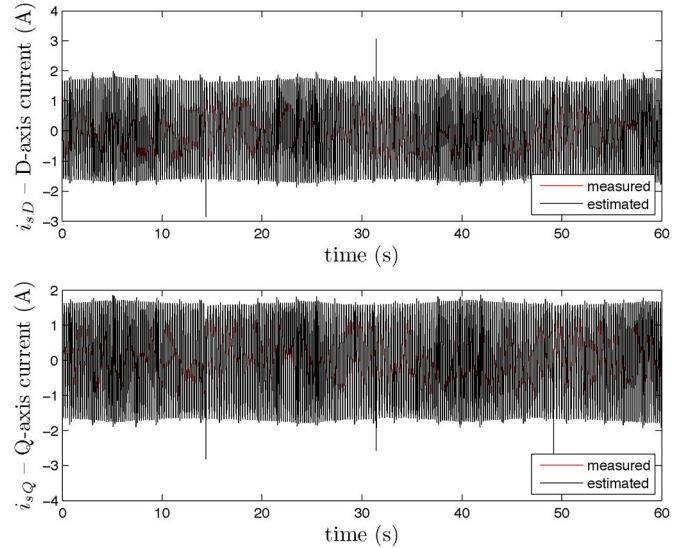


Fig. 18. i_{sD} , i_{sQ} estimated and measured current components during the 0.1 \rightarrow -0.1 step with the non-null gain matrix (experiment).

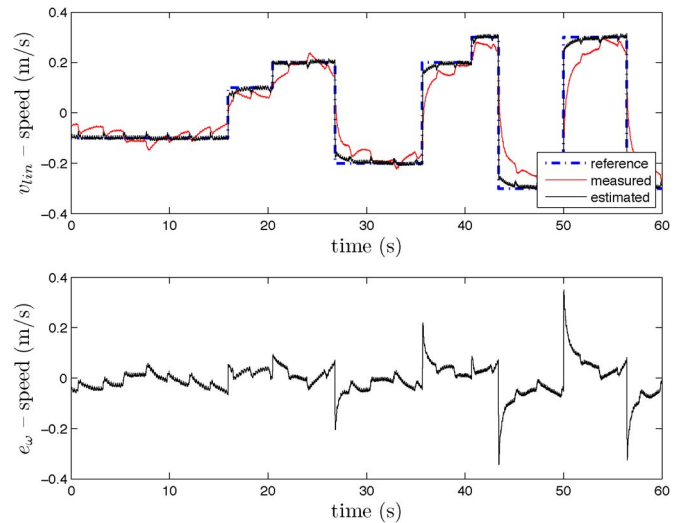


Fig. 19. Reference, estimated, and measured linear speeds during the -0.1 \rightarrow 0.1 \rightarrow 0.2 \rightarrow -0.2 \rightarrow 0.2 \rightarrow 0.3 \rightarrow -0.3 \rightarrow -0.3 \rightarrow -0.3 step test with the non-null gain matrix (experiment).

parameters curve track the time variation of the estimated speed. They present a quick variation at any transient speed step as well as a different steady-state value at each steady-state speed working condition.

C. Comparison With Other Observers

To verify the improvements achievable with the proposed TLS full-order Luenberger observer taking into consideration the LIM dynamic end effects, some experimental comparisons with other observers in the literature have been made. The adopted test setup is that described in Section V. In particular, the proposed observer has been compared with the TLS EXIN MRAS observer [8], the classic MRAS [9], and the SM-MRAS [10] observers. These three observers are all MRASs, based on the flux error minimization, so their comparison is consistent. While the TLS EXIN MRAS observer has been specifically

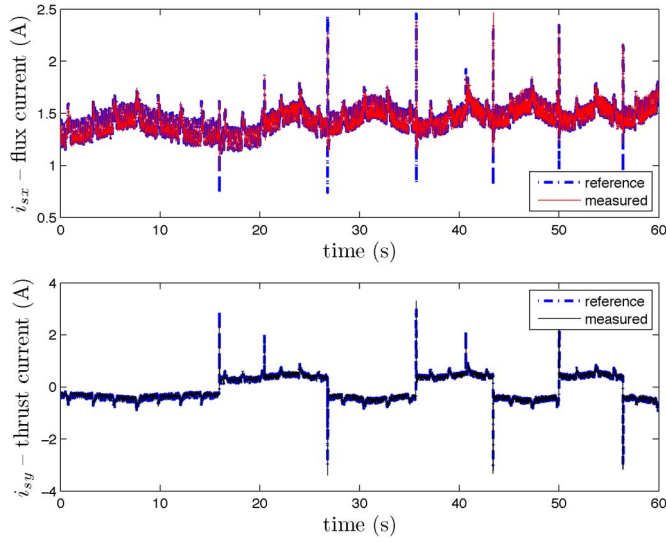


Fig. 20. i_{sx} , i_{sy} reference and measured current components during the $-0.1 \rightarrow 0.1 \rightarrow 0.2 \rightarrow -0.2 \rightarrow 0.2 \rightarrow 0.3 \rightarrow -0.3 \rightarrow -0.3 \rightarrow -0.3$ step test with the non-null gain matrix (experiment).

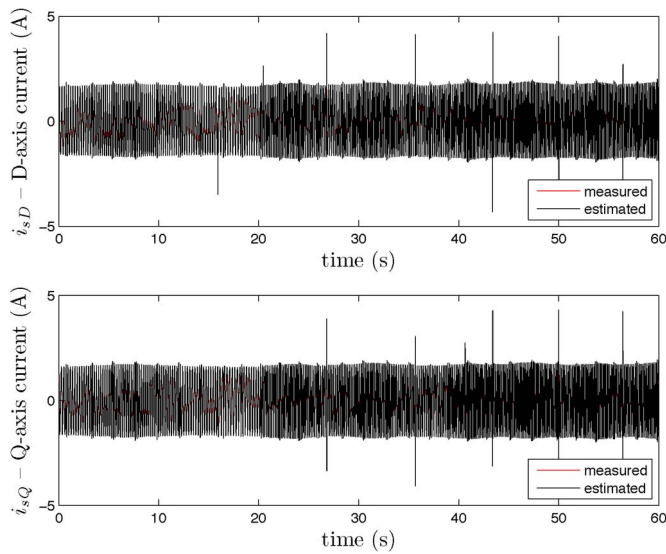


Fig. 21. i_{sD} , i_{sQ} estimated and measured current components during the $-0.1 \rightarrow 0.1 \rightarrow 0.2 \rightarrow -0.2 \rightarrow 0.2 \rightarrow 0.3 \rightarrow -0.3 \rightarrow -0.3 \rightarrow -0.3$ step test with the non-null gain matrix (experiment).

devised for LIM drives since it implicitly takes into consideration its dynamic end effects, the classic MRAS and the SM-MRAS have been originally devised for the RIM and just rearranged here to be adopted straightforwardly for the LIM.

As shown in [8], the TLS EXIN MRAS observer permits the speed control loop to be closed with the estimated speed, it does not need a low pass (LP) filter on the estimated speed, with the consequent increase of the observer bandwidth, and permits the drive to work down to 0.2 m/s. On the contrary, the straightforward application of the classic MRAS and SM-MRAS, devised for RIM, to the LIM does not permit the speed loop to be closed with the estimated speed. In such operating conditions, the drive behavior becomes unstable. The corresponding tests have therefore been made by closing the speed loop with the measured speed. These considerations fur-

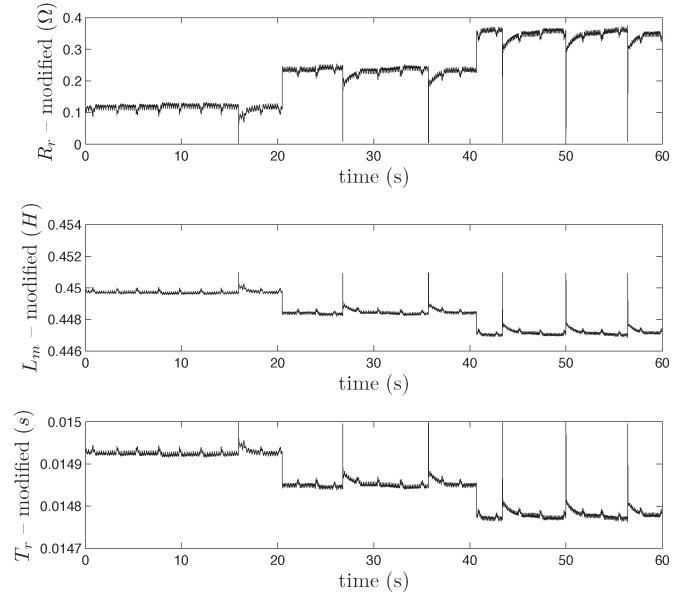


Fig. 22. Modified electrical parameters during the $-0.1 \rightarrow 0.1 \rightarrow 0.2 \rightarrow -0.2 \rightarrow 0.2 \rightarrow 0.3 \rightarrow -0.3 \rightarrow -0.3 \rightarrow -0.3$ step test with the non-null gain matrix (experiment).

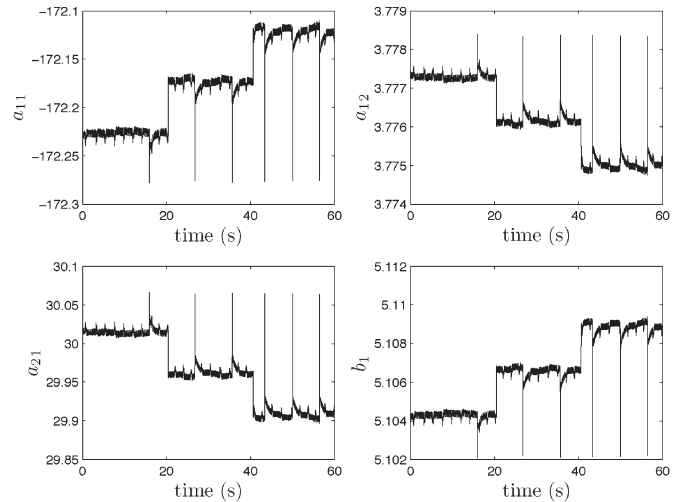


Fig. 23. Modified state model parameters during the $-0.1 \rightarrow 0.1 \rightarrow 0.2 \rightarrow -0.2 \rightarrow 0.2 \rightarrow 0.3 \rightarrow -0.3 \rightarrow -0.3 \rightarrow -0.3$ step test with the non-null gain matrix (experiment).

ther confirm the improvements achievable with both the proper modeling of LIM, considering the dynamic end effects, and the TLS EXIN training of the NN adaptive model. Moreover, both the classic MRAS and the SM-MRAS need an LP to filter the estimated speed, with the consequent strong reduction of the observer bandwidth.

In the following tests, the only parameter of the TLS EXIN algorithm to be tuned is the learning rate α , which has been selected on the basis of a tradeoff between the requirements of high dynamic performance and the limitation of the ripple of the estimated speed at steady state. The same logic has governed the choice of the proportional integral's parameter of the classic MRAS. As far as the SM-MRAS observer is concerned, Comanescu and Xu [10] have proposed two different variants, called single-manifold SM observer and double-manifold DB

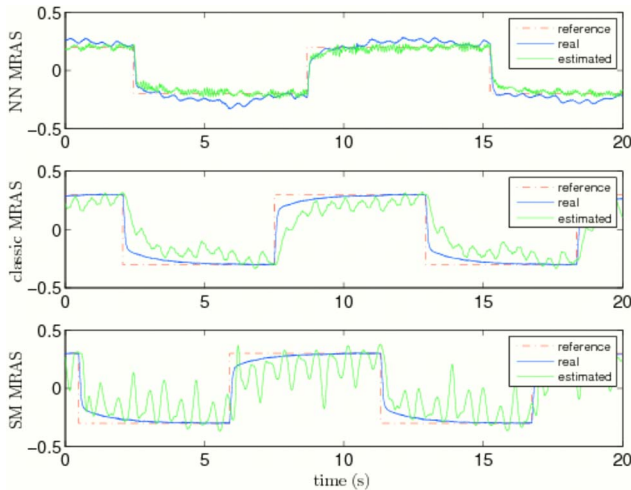


Fig. 24. Reference, estimated, and measured linear speeds with the TLS EXIN MRAS, the classic MRAS, and the SM-MRAS observers (experiments).

observer, respectively. In the following, the tests have been performed with the single-manifold SM-MRAS observer (see scheme in [10, Fig. 7]). Even in this case, the gain M of the observer has been chosen on the basis of a tradeoff between the stability issue and the dynamic performance issue.

Fig. 24 shows the reference, the measured, and the estimated speed, obtained with the aforementioned three observers, under speed square references of 0.2 m/s in the TLS EXIN MRAS case and 0.3 m/s in the classic MRAS and SM-MRAS cases. These are the minimum working speed for each of the aforementioned observers, taking into consideration that only the TLS EXIN MRAS is operated in closed-loop control. Table II compares the performance of each of them in terms of the following: the minimum working speed (referred to as the rated speed of the machine), the peak transient estimation error (referred to as the reference speed), the steady-state percent average estimation error (referred to as the reference speed), its corresponding standard deviation, and, finally, the standard deviations of the direct and quadrature components of the inductor currents. These last two parameters take into consideration the oscillations typically occurring in the electrical variables in sensorless drives at low speed (with the estimated speed fed back to the control loop). As a final result, the following statements can be concluded.

- 1) Among those tested, the only observers which can work in closed-loop speed control, at the tested speed, are the TLS full-order Luenberger and the TLS MRAS observer. The speed inversion with observers based on the RIM model is very critical and leads these observers to an unstable behavior.
- 2) The minimum working speed is obtained with the TLS full-order Luenberger: It corresponds to 1.4% of the rated speed with $\mathbf{G} \neq \mathbf{0}$ and to 2.95% of the rated speed with $\mathbf{G} = \mathbf{0}$. The TLS MRAS observer presents a minimum working speed equal to the 2.95%, as in the case of the TLS full-order Luenberger with $\mathbf{G} = \mathbf{0}$. Both the classic MRAS and SM-MRAS cannot work below 4.41% of the rated speed.

TABLE II
COMPARISON AMONG SEVERAL SPEED OBSERVERS

	TLS Luenberger ($\mathbf{G} \neq \mathbf{0}$)	TLS Luenberger ($\mathbf{G} = \mathbf{0}$)	TLS MRAS	Classic MRAS	SM-MRAS
minimum speed (% rated speed)	1.4	2.95	2.95	4.41	4.41
speed mean error (%)	37	20	22	33	33
speed peak error (%)	120	50	90	133	160
speed standard deviation	$6.5 \cdot 10^{-3}$	$1.3 \cdot 10^{-2}$	$2.1 \cdot 10^{-2}$	$4.2 \cdot 10^{-2}$	$1.2 \cdot 10^{-1}$
i_{sx} standard deviation	$9.44 \cdot 10^{-2}$	$1.4 \cdot 10^{-1}$	$2.7 \cdot 10^{-1}$	\	\
i_{sy} standard deviation	$1.15 \cdot 10^{-1}$	$1.5 \cdot 10^{-1}$	$3.4 \cdot 10^{-1}$	\	\

- 3) At the minimum working speed, the average estimation error with the TLS full-order Luenberger observer is about 37% with $\mathbf{G} \neq \mathbf{0}$ and 20% with $\mathbf{G} = \mathbf{0}$. The corresponding average estimation error with the TLS MRAS observer is almost equal (22%), while those obtained with the classic MRAS and SM-MRAS are around 30%. This accounts for a better accuracy in the steady-state speed estimation achievable by adopting any of the NN-based observers and particularly adopting a modelization accounting for the dynamic end effects.
- 4) During the speed reversal at the minimum working speed, the lowest peak estimation error is achieved by the TLS EXIN Luenberger with $\mathbf{G} = \mathbf{0}$ (50%), followed by the TLS MRAS (90%), the TLS EXIN Luenberger with $\mathbf{G} \neq \mathbf{0}$ (120%), the classic MRAS (133%), and, finally, the SM-MRAS (160%). It should be remarked that the slightly higher peak estimation error of the TLS EXIN Luenberger with $\mathbf{G} \neq \mathbf{0}$ is to be justified by the fact that the working speed is far lower than the others. This explains the better accuracy in transient speed achievable with the TLS EXIN Luenberger.
- 5) At the minimum working speed, the standard deviation obtainable with the TLS full-order Luenberger observer with $\mathbf{G} \neq \mathbf{0}$ is 1/2 of that with $\mathbf{G} = \mathbf{0}$, 1/4 of that with the TLS MRAS, 1/8 of that with the classic MRAS, and 1/10 of that with the SM-MRAS. This explains the closest speed estimation to the measured value during the steady-state phase and for the corresponding lower oscillations achievable with the TLS full-order Luenberger.
- 6) The standard deviations of the i_{sx} , i_{sy} current components achievable with TLS full-order Luenberger, slightly lower in the case of $\mathbf{G} \neq \mathbf{0}$ than in the case of $\mathbf{G} = \mathbf{0}$, are almost 1/2 of those with the TLS MRAS. This explains the lower oscillation of the flux and thrust of the machine at steady state and, in particular, for a lower sensitivity to saturation phenomena in the machine. No values are present for the classic MRAS and SM-MRAS since, in this case, the measured speed has been fed back

to the speed control loop, and therefore, this effect is not apparent.

VII. CONCLUSION

This paper has proposed a neural based full-order Luenberger adaptive speed observer for LIM drives, where the linear speed is estimated on the basis of the TLS EXIN linear neuron. In this respect, a novel state space-vector representation of the LIM has been deduced, taking into consideration the LIM dynamic end effects. Starting from this standpoint, the state equations of the LIM have been discretized and rearranged in a matrix form to be solved, in terms of the LIM linear speed, by any LS technique. Because of the nature of the matrix equation to be addressed, the problem has been faced up to as an orthogonal regression one. The TLS EXIN neuron has been used to compute online, in recursive form, the machine linear speed since it is the only NN able to solve online, in a recursive form, a TLS problem. A new gain matrix choice of the Luenberger observer, specifically taking into consideration the LIM end effects, has been proposed. The TLS full-order Luenberger adaptive speed observer described here has been tested experimentally on a suitably developed test setup. It has been further compared with the TLS EXIN MRAS, the classic MRAS, and the SM-MRAS observers. Results show that the sensorless LIM drive overcomes the other in the following aspects.

- 1) It can work in closed-loop speed control, as TLS EXIN MRAS, differently from the classic MRAS and the SM-MRAS observers.
- 2) It presents the lowest minimum working speed, equal to 1.4% of the rated speed obtained with a non-null gain matrix, whereas the minimum working speed of the TLS EXIN MRAS is 2.95% and that of the classic MRAS and the SM-MRAS observers is 4.41%.
- 3) It presents the lowest peak estimation error during the low speed inversion test, equal to 50% of the reference speed, followed by the TLS EXIN MRAS with 90%, the classic MRAS with 133%, and, finally, the SM-MRAS with 160%.
- 4) It presents the lowest value of standard deviation of the speed, as well as of the i_{sx} , i_{sy} current components, accounting for lower oscillations of the electrical variables occurring in speed closed-loop control.

APPENDIX

DERIVATION OF MATRIX EQUATION (20)

The first two scalar equations of the matrix (11) can be written as

$$\begin{cases} \frac{di_{sD}}{dt} = \hat{a}_{11}i_{sD} + \hat{a}_{12} \left(\frac{1}{T_r} + \frac{\hat{R}_r}{L_m} \right) \hat{\psi}_{rd} + \hat{a}_{12} \frac{p\pi}{\tau_p} \hat{v} \hat{\psi}_{rq} + \hat{b}u_{sD} \\ \frac{di_{sQ}}{dt} = \hat{a}_{11}i_{sQ} + \hat{a}_{12} \left(\frac{1}{T_r} + \frac{\hat{R}_r}{L_m} \right) \hat{\psi}_{rq} - \hat{a}_{12} \frac{p\pi}{\tau_p} \hat{v} \hat{\psi}_{rd} + \hat{b}u_{sQ} \end{cases} \quad (I.1)$$

where the current components are measured variables and the rotor flux and speed are estimated ones. Moving from the continuous domain to the discrete one and approx-

imating the continuous derivative with the discrete filter $((1 - Z^{-1})/(T_s Z^{-1}))$, where T_s is the sampling time of the control systems, the following equations can be deduced:

$$\begin{cases} \frac{i_{sD}(k) - i_{sD}(k-1)}{T_s} = \hat{a}_{11}i_{sD}(k-1) + \hat{a}_{12} \left(\frac{1}{T_r} + \frac{\hat{R}_r}{L_m} \right) \hat{\psi}_{rd}(k-1) \\ \quad + \hat{a}_{12} \frac{p\pi}{\tau_p} \hat{v}(k-1) \hat{\psi}_{rq}(k-1) + \hat{b}u_{sD}(k-1) \\ \frac{i_{sQ}(k) - i_{sQ}(k-1)}{T_s} = \hat{a}_{11}i_{sQ}(k-1) + \hat{a}_{12} \left(\frac{1}{T_r} + \frac{\hat{R}_r}{L_m} \right) \hat{\psi}_{rq}(k-1) \\ \quad - \hat{a}_{12} \frac{p\pi}{\tau_p} \hat{v}(k-1) \hat{\psi}_{rd}(k-1) + \hat{b}u_{sQ}(k-1) \end{cases} \quad (I.2)$$

where k is the current time sample. From (I.2), the matrix equation (20) can be easily deduced.

REFERENCES

- [1] I. Boldea and S. Nasar, *Linear Electric Motors*. Englewood Cliffs, NJ, USA: Prentice-Hall, 1987.
- [2] I. Boldea and S. A. Nasar, *Linear Electric Actuators and Generators*. Cambridge, U.K.: Cambridge Univ. Press, 1997.
- [3] K. Rajashekhara, A. Kawamura, and K. Matsuse, *Sensorless Control of AC Motor Drives*. Piscataway, NJ: IEEE Press, 1996.
- [4] J. Holtz, "Sensorless control of induction motor drives," *Proc. IEEE*, vol. 90, no. 8, pp. 1359–1394, Aug. 2002.
- [5] C.-I. Huang, F. Li-Chen, W.-Y. Jywe, and J. C. Shen, "Speed motion-sensorless with adaptive control approach of linear induction motor unknown resistance and payload," in *Proc. IEEE PESC*, Jun. 15–19, 2008, pp. 3887–3893.
- [6] H.-M. Ryu, J.-I. Ha, and S.-K. Sul, "A new sensorless control thrust control of linear induction motor," in *Conf. Rec. IEEE IAS Annu. Meeting*, 2000, vol. 3, pp. 1655–1661.
- [7] M. Cirrincione, M. Pucci, A. Sferlazza, and G. Vitale, "Neural based MRAS sensorless techniques for high performance linear induction motor drives," in *Proc. 36th Annu. IEEE IECON*, Nov. 7–10, 2010, pp. 918–926.
- [8] A. Accetta, M. Cirrincione, M. Pucci, and G. Vitale, "MRAS speed observer for high performance linear induction motor drives based on linear neural networks," *IEEE Trans. Power Electron.*, vol. 28, no. 1, pp. 123–134, Jan. 2013.
- [9] C. Shauder, "Adaptive speed identification for vector control of induction motors without rotational transducers," *IEEE Trans. Ind. Appl.*, vol. 28, no. 5, pp. 1054–1061, Sep./Oct. 1992.
- [10] M. Comanescu and L. Xu, "Sliding-mode MRAS speed estimators for sensorless vector control of induction machine," *IEEE Trans. Ind. Electron.*, vol. 53, no. 1, pp. 146–153, Feb. 2006.
- [11] M. Cirrincione, M. Pucci, G. Cirrincione, and G. Capolino, "An adaptive speed observer based on a new total least-squares neuron for induction machine drives," *IEEE Trans. Ind. Appl.*, vol. 42, no. 1, pp. 89–104, Jan./Feb. 2006.
- [12] M. Cirrincione, M. Pucci, G. Cirrincione, and G. Capolino, "Sensorless control of induction machines by a new neural algorithm: The TLS EXIN neuron," *IEEE Trans. Ind. Electron.*, vol. 54, no. 1, pp. 127–149, Feb. 2007.
- [13] M. Cirrincione, M. Pucci, and G. Vitale, *Power Converters and AC Electrical Drives with Linear Neural Networks (Energy, Power Electronics, and Machines)*, A. Emadi, Ed., 1st ed. New York, NY, USA: Taylor & Francis, May 14, 2012.
- [14] J. Duncan, "Linear induction motor-equivalent-circuit model," *Proc. Inst. Elect. Eng.—Elect. Power Appl.*, vol. 130, pt. B, no. 1, pp. 51–57, Jan. 1983.
- [15] H. Kubota, K. Matsuse, and T. Nakano, "DSP-based speed adaptive flux observer of induction motor," *IEEE Trans. Ind. Appl.*, vol. 29, no. 2, pp. 344–348, Mar./Apr. 1993.
- [16] G. Cirrincione, M. Cirrincione, J. Héroult, and S. Van Huffel, "The MCA EXIN neuron for the minor component analysis: Fundamentals and comparisons," *IEEE Trans. Neural Netw.*, vol. 13, no. 1, pp. 160–187, Jan. 2001.
- [17] G. Cirrincione and M. Cirrincione, *Neural-Based Orthogonal Data Fitting: The EXIN Neural Networks*. Hoboken, NJ, USA: Wiley, 2010.
- [18] J. H. Sung and K. Nam, "A new approach to vector control for a linear induction motor considering end effects," in *Conf. Rec. IEEE IAS Annu. Meeting*, 1999, vol. 4, pp. 2284–2289.
- [19] G. Kang and K. Nam, "Field-oriented control scheme for linear induction motor with the end effect," *Proc. Inst. Elect. Eng.—Elect. Power Appl.*, vol. 152, no. 6, pp. 1565–1572, Nov. 2005.
- [20] V. Isastia, G. Gentile, S. Meo, A. Ometto, N. Rotondale, and M. Scarano, "A voltage feeding algorithm for vectorial control of linear asynchronous

machines taking into account end effect,” in *Proc. Power Electron. Drives Energy Syst. Ind. Growth*, 1998, vol. 2, pp. 729–734.

- [21] I. Takahashi and Y. Ide, “Decoupling control of thrust and attractive force of a LIM using a space vector control inverter,” *IEEE Trans. Ind. Appl.*, vol. 29, no. 1, pp. 161–167, Jan./Feb. 1993.
- [22] J. Holtz and J. Quan, “Sensorless vector control of induction motors at very low speed using a nonlinear inverter model and parameter identification,” *IEEE Trans. Ind. Appl.*, vol. 38, no. 4, pp. 1087–1095, Jul./Aug. 2002.
- [23] J. Holtz and J. Quan, “Drift- and parameter-compensated flux estimator for persistent zero-stator-frequency operation of sensorless-controlled induction motors,” *IEEE Trans. Ind. Appl.*, vol. 39, no. 4, pp. 1052–1060, Jul./Aug. 2003.



Angelo Accetta (M'08) received the Laurea degree in electrical engineering from the University of Palermo, Palermo, Italy, in 2008, where he received the Ph.D. degree in electrical engineering in 2011, from the Department of Electrical Engineering, Electronics and Telecommunications.

He is currently a Researcher at the Section of Palermo of ISSIA-CNR (Institute on Intelligent Systems for Automation), Palermo, Italy. His current research interests are electrical machines, control techniques of electrical drives, intelligent control,

power converters, and fuel cell system control and diagnosis.



Maurizio Cirrincione (SM'03) received the “Laurea” degree from the Politecnico di Torino, Turin, Italy, in 1991, and the Ph.D. degree from the University of Palermo, Palermo, Italy, in 1996, both in electrical engineering.

From 1996 to 2005 he was a Researcher with the I.S.S.I.A.-C.N.R. Section of Palermo (Institute on Intelligent Systems for Automation), Palermo, Italy. Since 2005 he has been a Full Professor of Control Systems at the UTBM (University of Technology of Belfort-Montbéliard) in Belfort, France, and a

member of the IRTES Laboratory and the FCLab (Fuel Cell laboratory) in Belfort, France. Since April 2014, he has been the Head of the School of Engineering and Physics of the University of the South Pacific in Suva, Fiji Islands. His current research interests are neural networks for modeling and control, system identification, intelligent control, power electronics, power quality, renewable energy systems, control of fuel cell systems, hybrid vehicles, and electrical machines and drives with rotating or linear ac motors. He is the author of over 140 papers, 50 of which were published in high impact factor journals, and of two books.

Prof. Cirrincione was awarded the 1997 “E.R.Caianello” prize for the best Italian Ph.D. thesis on neural networks.



Marcello Pucci (M'03–SM'11) received the “Laurea” and Ph.D. degrees in electrical engineering from the University of Palermo, Palermo, Italy, in 1997 and 2002, respectively.

In 2000, he was a host student at the Institute of Automatic Control, Technical University of Braunschweig, Braunschweig, Germany, working in the field of control of ac machines, with a grant from the Deutscher Akademischer Austauschdienst—German Academic Exchange Service. He was a Researcher from 2001 to 2007 and has been a Senior Researcher since 2008 at the Section of Palermo of ISSIA-CNR (Institute on Intelligent Systems for Automation), Palermo, Italy. His current research interests are electrical machines, the control, diagnosis, and identification techniques of electrical drives, intelligent control, and power converters.

Dr. Pucci serves as an Associate Editor of the IEEE TRANSACTIONS ON INDUSTRIAL ELECTRONICS and the IEEE TRANSACTIONS ON INDUSTRY APPLICATIONS. He is a member of the Editorial Board of the *Journal of Electrical Systems*.



Gianpaolo Vitale (M'04–SM'12) received the M.Sc. degree in electronic engineering from the University of Palermo, Palermo, Italy, in 1988.

From 1994 to 2001, he was a Researcher, and since 2002, he has been a Senior Researcher with the CNR at the Institute of Intelligent Systems for Automation (ISSIA), section of Palermo. He has been the Supervisor of a research project on electromagnetic compatibility of electric drives and of a research project on intelligent management of electric energy supplied by renewable sources. He is Professor of

Power Electronics at the University of Palermo, Faculty of Engineering. His current research interests are in the fields of power electronics and related problems of electromagnetic compatibility.

Prof. Vitale is a member of the IEEE Vehicular Technology Society, IEEE Industrial Electronics Society, and IEEE Electromagnetic Compatibility Society, and he serves as a reviewer for several journals and conferences.